Device

Article

An artificial olfactory sensory neuron for selective gas detection with in-sensor computing

Graphical abstract

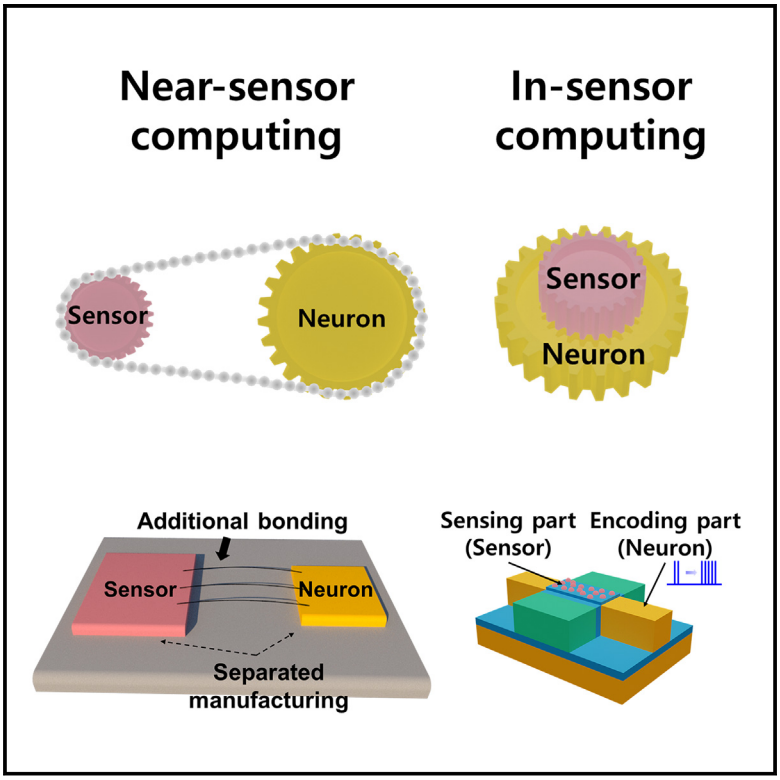

Highlights

- An artificial olfactory neuron is developed for detecting different gases
- The single transistor functions as a sensor and a neuron for a neuromorphic system
- The two-in-one device removes the need for external processors or memory units
- The multi-functional hardware reduces power requirements and form factor

Authors

Sang-Won Lee, Mingu Kang, Joon-Kyu Han, Seong-Yun Yun, Inkyu Park, Yang-Kyu Choi

Correspondence

inkyu@kaist.ac.kr (I.P.), ykchoi@ee.kaist.ac.kr (Y.-K.C.)

In brief

We demonstrate in-sensor computing hardware with a sensory neuron and a synapse for selective gas classification. This sensory neuron, with a two-in-one type, combines a neuron for a spiking neural network (SNN) and a sensor for gas detection. The sensory neuron and the synapse are silicon transistors, which offer advantages for large-scale integration with high throughput, aided by matured silicon fabrications. The proposed hardware is attractive for reducing power consumption and footprint due to its spiking nature and two-in-one structure, respectively.

Lee et al., 2023, Device *1*, 100063
September 22, 2023
https://doi.org/10.1016/j.device.2023.100063

CellPress

Please cite this article in press as: Lee et al., An artificial olfactory sensory neuron for selective gas detection with in-sensor computing, Device (2023), https://doi.org/10.1016/j.device.2023.100063

Device

CellPress

Article

An artificial olfactory sensory neuron for selective gas detection with in-sensor computing

Sang-Won Lee,[1] Mingu Kang,[2] Joon-Kyu Han,[1] Seong-Yun Yun,[1] Inkyu Park,[2,*] and Yang-Kyu Choi[1,3,*]
[1]School of Electrical Engineering, Korea Advanced Institute of Science and Technology (KAIST), 291 Daehak-ro, Yuseong-gu, Daejeon 34141, Republic of Korea
[2]Department of Mechanical Engineering, Korea Advanced Institute of Science and Technology (KAIST), 291 Daehak-ro, Yuseong-gu, Daejeon 34141, Republic of Korea
[3]Lead contact
*Correspondence: inkyu@kaist.ac.kr (I.P.), ykchoi@ee.kaist.ac.kr (Y.-K.C.)
https://doi.org/10.1016/j.device.2023.100063

THE BIGGER PICTURE With the advent of the IoT era, in-sensor computing, which can perform both sensing and local data processing in a sensor, becomes increasingly important because it can reduce power consumption and footprint area. Herein, an olfactory module has been developed to sense and distinguish different gases. The design is composed of two sensory neurons and four synapses for neuromorphic hardware with a spiking neural network that can function without the direct engagement of an external processor. Each sensory neuron combines a sensor and a neuron, which is advantageous for further reducing power consumption due to its inherent two-in-one nature and spiking behavior. The configuration of a single-layer perceptron (SLP) in this work can be extended to that of a multi-layer perceptron (MLP) for classifying a more diverse gas mixture with the aid of silicon microfabrication, which provides large-scale integration with high throughput and low cost.

SUMMARY

We present a neuromorphic sensory module for gas detection using a two-in-one typed olfactory neuron for in-sensor computing. The module integrates a sensor for gas detection and a neuron for generating spike signals and delivering them into the post-synapse. The sensing ability is enabled by catalytic metal particles on a silicon nanowire field-effect transistor (Si-NW FET), while the neuronal ability is also realized by the Si-NW FET itself, which encodes spike signals for a spiking neural network (SNN). By mounting palladium (Pd) and platinum (Pt) nanoparticles on the Si-NW FET, we demonstrate the module to classify H_2 and NH_3 using a single-layer perceptron (SLP) with the sensory neurons and FET-based synapses. Power demand and manufacturing cost efficiency are important considerations in mobile applications and edge computing in the Internet-of-Things era. This in-sensor module-based SNN hardware provides a cost-effective solution that is inherently more power and form-factor efficient over existing designs.

INTRODUCTION

Gas sensors are widely utilized for industrial safety, healthcare, food analysis, and national security.[1–5] For many applications, small, portable gas sensors are preferred, especially given the rising interest and investment in the Internet of Things (IoT).[6,7] As a good gas sensor, various sensor metrics, such as sensitivity to detect a small amount of gas, selectivity to identify a specific gas, and reliability to reproduce the same response for long-term use, should be ensured to be as high as possible.[8–10] In particular, selectivity with low-power consumption as well as a fast response time is critical to distinguish various gases. There have been many attempts to classify different gases using a sensor array, such as in the form of an electronic nose (e-nose) that mimics a biological nose.[11–15] Although there have been numerous gas sensors developed to identify specific gases using dedicated sensor materials, a considerable amount of this research relies on post-data processing, such as a deep neural network (DNN), which limits their functionalities and efficiencies because of the demand for processing power and the subsequent energy demand.[16]

There are three types of design architectures for sensors: conventional computing, near-sensing computing, and in-sensor computing.[17] Conventional computing is composed of

Please cite this article in press as: Lee et al., An artificial olfactory sensory neuron for selective gas detection with in-sensor computing, Device (2023), https://doi.org/10.1016/j.device.2023.100063

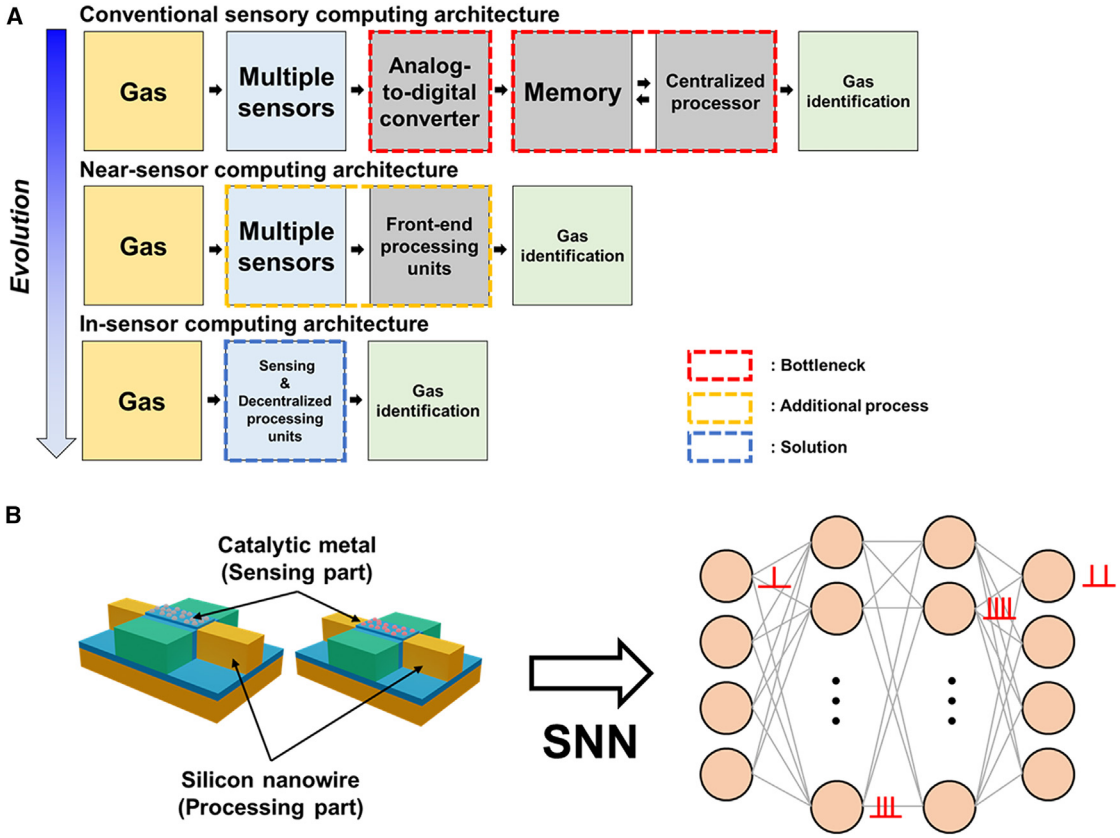

Figure 1. In-sensor computing architecture based on a spiking neural network (SNN) with the proposed Si-NW FET enclosing catalytic metal particles

(A) Block diagram of the sensory computing architecture for gas identification. The conventional sensory computing architecture has a bottleneck arising from the von-Neumann architecture. The near-sensor computing architecture requires an additional process for the interconnection between the sensing units and the processing units. The disadvantages of the high processing cost and energy consumption can be resolved using the in-sensor computing architecture.

(B) Schematic of different catalytic metal-particle-embedded Si-NW FETs for the in-sensor computing architecture. A Si-NW FET generates spike signals as an artificial sensory neuron for the SNN, while the catalytic metal particles on it respond to a specific gas.

a multiple-sensor array, an analog-to-digital converter (ADC), memory, and a centralized processor unit to perform heavy computations. Near-sensing computing is comprised of a multiple-sensor array and semi-decentralized front-end processing units to perform intermediate computations. Unlike the other two, in-sensor computing uses a multi-sensor array that encloses decentralized processing cores to perform computations in the form of a single unit. Therefore, in terms of miniaturization and power efficiency, there is an inherent advantage for the in-sensor computing approach over the other two architectures.

In conventional computing architecture, power consumption is a serious concern due to the use of an ADC. Additionally, extra power is consumed during DNN-based computation when processing digital signals from the ADC in a processing unit, temporarily storing them in a memory unit, and reloading them back into the processing unit for subsequent computation. This serial processing is inevitable in the von Neumann computing architecture. Consequently, the conventional computing architecture consumes a significant amount of power owing to repeated data processing and transferring (see Figure 1A). This is undesirable for IoT devices, which have an emphasis on low power consumption and small size. Unlike the conventional computing architecture, the near-sensor or in-sensor computing architecture adopts a spiking neural network (SNN) that works by mimicking a biological sensory system and overcomes the above issues related to DNN-based computations, as the architecture does not require heavy post-processing units (see Figure 1A).

SNNs can be built using multi-layer perceptron (MLP), which consists of an artificial neuron and a synapse. The neurons produce spikes as output signals, while the synapses determine the connectivity between neuron layers. Owing to their low power consumption and reduced footprint, the sensory architecture with SNNs is advantageous for mobile and IoT sensors.[18–20] However, previous studies that implemented the SNN architecture had an unresolved limitation because the sensing units and spiking neurons were still separate.[21,22] Additional manufacturing processes, such as packaging or wire bonding, are required to connect the sensing units and spiking neurons, but they can increase power consumption, processing time delay, and manufacturing cost. On the other hand, the metal-oxide-semiconductor field-effect transistor (MOSFET), a key element of complementary MOS (CMOS) technology, has advanced microelectronics and led to

Please cite this article in press as: Lee et al., An artificial olfactory sensory neuron for selective gas detection with in-sensor computing, Device (2023), https://doi.org/10.1016/j.device.2023.100063

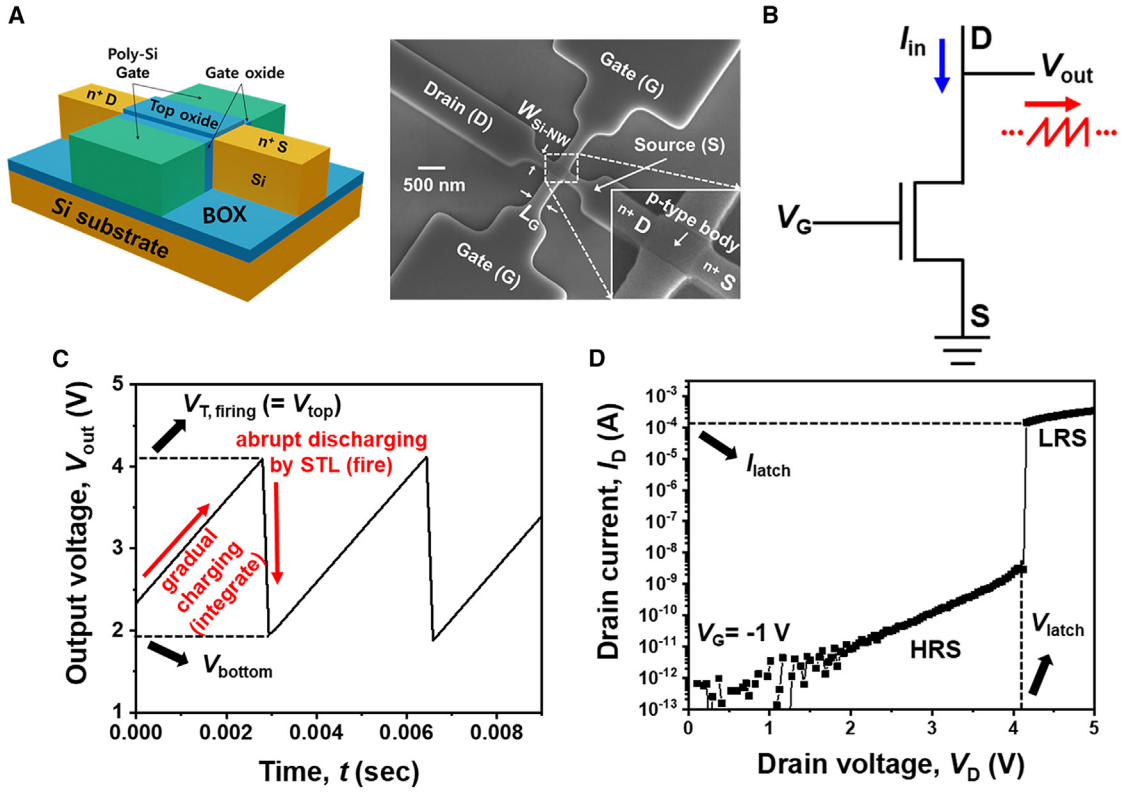

Figure 2. Measured electrical characteristics from the fabricated Si-NW FET with the corresponding symbolic representation and SEM photograph before embedding catalytic metal

(A) Schematic of the Si-NW FET and its SEM image.

(B) Symbolic representation of the Si-NW FET. V_{out} with a wedge shape was produced from D when I_{in} was applied to D under the condition of a V_G value smaller than V_T.

(C) Wedge-shaped spiking characteristic (V_{out}-time) of the Si-NW FET, showing the integrate-and-fire behavior of the neuron.

(D) I_D-V_D characteristics of the Si-NW FET. An abrupt increase of I_D occurs when V_D reaches V_{latch} due to the single-transistor latch (STL), which converts a high resistance state (HRS) to a low resistance state (LRS). I_{latch} flows at V_{latch}.

revolutionary changes in information and communication technology. If sensor technology adopts and actively utilizes CMOS technology, it should be straightforward to enable mass production due to the well-established commercial CMOS technology. Furthermore, it is highly desirable for a sensor to directly produce an electrical signal that responds to non-electrical signals from introduced analytes, without the aid of a transducer or an ADC. If sensor technology can ride the wave of this technology trend, a single MOSFET without the need for a transducer or an ADC must be modified to act as both a sensor and a spiking neuron, representing a new frontier that has not been adequately explored thus far.

In this work, we demonstrate an olfactory sensory neuron that can detect several different gases using an in-sensor computing architecture, going beyond our previous work with the near-sensor computing architecture.[21] This sensory neuron has a two-in-one structure and acts as both a sensor and a neuron, as shown in Figure 1B. To produce spiking signals for a neuronal function, we used a silicon nanowire MOSFET (Si-NW FET), which is similar to a fin-shaped FET (FinFET). Unlike a conventional FinFET, where a folded gate (G) wraps two sidewalls and the top of a protruding fin-shaped Si-NW, the new design exposes the top of the Si-NW by separating the folded G using chemical mechanical polishing (CMP), as shown in Figure 2A. This Si-NW neuron is composed of a heavily doped n^+ source (S), a moderately doped p-type body, and a heavily doped n^+ drain (D) along the channel direction. To detect a gas, two different catalytic metal nanoparticles of palladium (Pd) and platinum (Pt) reacting with two gases are formed on the exposed Si-NW. By combining these two sensory neurons and four synapses made of another MOSFET for a single-layer perceptron (SLP) configuration, the final module can quantitatively detect the presence of two gases: hydrogen (H_2) and ammonia (NH_3). As a bio-mimicry e-nose, this array, configured with 100% MOSFETs, can be developed further for a breath monitoring system to diagnose diseases.[23,24]

RESULTS

Structure of the Si-NW FET

The Si-NW FETs were fabricated on a p-type 8-inch silicon-on-insulator (SOI) wafer with a crystal orientation of (100), a top

Please cite this article in press as: Lee et al., An artificial olfactory sensory neuron for selective gas detection with in-sensor computing, Device (2023), https://doi.org/10.1016/j.device.2023.100063

silicon thickness of 55 nm (SOITEC), and a buried oxide (BOX) thickness of 145 nm. The folded G was separated, meaning that the p-type body was exposed with the n^+ S/D, which were not covered by the G. The nominal dimensions of the Si-NW FETs are an NW width ($W_{Si\text{-}NW}$) of 250 nm and a G length (L_G) of 300 nm, as shown in the scanning electron microscopy (SEM) image in Figure 2A. Pd and Pt nanoparticles were physically deposited across the Si-NW from n^+ S via the p-type body to the n^+ D. It should be noted that only metal nanoparticles located on the p-type body function electrically, and those situated on the n^+ S/D electrode do not have electrical performance (additional fabrication details are included in Figure S1).

Characteristics of Si-NW FET for neuronal behaviors

The proposed Si-NW FET for a sensory neuron has two modes. In the first, it functions as a typical MOSFET that incorporates voltage input and current output. The second mode is an oscillating neuron mode with current input and voltage output, as depicted in Figure 2B. When constant current (I_{in}) is fed to D with properly biased S and G, the sensory neuron produces a wedge-shaped oscillating output voltage (V_{out}) of a spiking signal, as shown in Figure 2C. It should be noted that V_{out} directly comes out from the Si-NW sensory neuron without the aid of a transducer or any external converting circuits. The spiking (or firing of the signal) caused by a single-transistor latch (STL) as shown in Figure 2D. An STL, which was frequently observed in a floating body (FB) FET, occurs when the D voltage (V_D) approaches the latch voltage (V_{latch}), as shown in Figure 2D.[25–28] In the wedge-shaped oscillating V_{out} in Figures 2C and 2A, a linearly increasing zone is dominated by a charging process to the FB, and an abruptly decreasing zone is governed by a discharging process from the FB (for more information on the iterative wedge-shaped oscillating V_{out}, one may refer to the energy band diagrams in Figure S2).

When I_{in} is fed to D of the Si-NW FET, the following sequential process occurs: (1) the built-in potential in D ($V_{bi,D}$) is enlarged; (2) impact ionization to generate electron and hole pairs is triggered due to injected electrons from S with the increased $V_{bi,D}$; (3) the created holes accumulate in the p-type FB; (4) the built-in potential in S ($V_{bi,S}$) is accordingly lowered; (5) more electrons are injected into the p-type FB; (6) the impact ionization is boosted and the additionally generated holes pile in the p-type FB as a gradual charging (integrating) process, with a linear incremental slope; and (7) $V_{bi,S}$ is reduced further and numerous electrons are injected to the p-type FB, with the Si-NW becoming more conductive. During this step, $V_{bi,D}$ is abruptly reduced by the injected electrons, and the V_{out} is emitted from D with a wedge shape as an abrupt discharging (firing) process. The accumulated holes in the FB escape toward S, and the output current (I_{out}) flows out from S as a spike. Finally, (8) $V_{bi,S}$ and $V_{bi,D}$ tend toward their initial resting states and the Si-NW becomes very resistive in an automatic resetting process. The entire sequential process from (1) to (8) creates a positive feedback loop because the volume of the channel in the Si-NW FET where the generated holes are accumulated is finite, while carriers are continuously supplied to the Si-NW FET in the form of I_{in}. Here, step (7), which causes I_D to abruptly increase to I_{latch} in Figure 2D, is the STL.

Figure 2D shows the I_D-V_D characteristics of the Si-NW FET. The two separate G voltages (V_G) were both set to −1 V to turn off the Si-NW FET before the STL. This was done because sustaining an off state is advantageous for accumulating holes in the FB. When V_D reaches V_{latch}, I_D increases abruptly to the latch current (I_{latch}) due to the STL. A typical characteristic of an artificial neuron is its leaky integrate-and-fire (LIF) operation, similar to that of a biological neuron. The charging process corresponds to "integrate," while the abrupt discharging by the STL corresponds to "fire." The "leaky" characteristic in a MOSFET with an FB, which is not used in this work, was demonstrated in our previous works.[26] The V_{out}-time (t) characteristic in Figure 2C shows the neuronal LIF operation, with the linear slope in the incremental V_{out} proportional to I_{in} at a fixed value of spiking frequency (f). This f is modeled with the following equation:

$$f = \frac{I_{in}}{C_{par} \cdot (V_{T,firing} - V_{bottom})} \quad \text{(Equation 1)}$$

where $V_{T,firing}$ is the peak voltage at the moment of firing, V_{bottom} is the base voltage prior to charging that corresponds to the resting voltage, and C_{par} represents all capacitances involved in the measurements. These are the FB capacitance itself, the probing pad capacitance, and the equipment capacitance, including the cable capacitance.[29,30]

Once I_{in} and C_{par} are fixed, f increases as $V_{T,\ firing}$ decreases and as V_{bottom} increases. In other words, the proposed sensory neuron can mimic a human olfactory neuron by adjusting f with $V_{T,firing}$ and V_{bottom} when a gas is introduced. This iterative integrating and firing operation generates an oscillatory V_{out} as long as I_{in} is supplied to the Si-NW FET, which is equivalent to a typical spiking characteristic of a biological neuron. Here, $V_{T,firing}$ corresponds to V_{latch} at the moment when the integrated charges flow out toward S under neuronal firing.[28] Additionally, V_{bottom}, which is determined by I_{latch}, corresponds to the resting voltage.

Measurement setup for gas detection

A hermetic gas chamber enclosing an electrical probing system was used to characterize the gas response directly. The electrical probing system used in this case was connected to a semiconductor parameter analyzer (model 4156C, Keysight) located outside the chamber. To control the gas concentrations of each of the gases, individual mass flow controllers (MFCs) regulated by Labview (National Instruments, Austin, TX, USA) software were used. Both targeted gases of H_2 and NH_3 (i.e., reacting gases) were sufficiently diluted with nitrogen (N_2) for safety. As a reference, the dilution of H_2 was 20,000 ppm in N_2, and that of NH_3 was 100 ppm in N_2. The reacting gases, H_2 or NH_3, were injected into the hermetic reacting chamber with the dilution gas, N_2, while maintaining a total flow rate of 400 sccm. A concentration of reacting gas was modulated by changing the ratio of each flow rate within total flow rate of 400 sccm. In addition, oxygen gas (O_2) flowing at 100 sccm was injected into the chamber to mimic an air environment composed of 80% N_2 and 20% O_2. The overall measurement apparatus is shown in Figure S3.

Please cite this article in press as: Lee et al., An artificial olfactory sensory neuron for selective gas detection with in-sensor computing, Device (2023), https://doi.org/10.1016/j.device.2023.100063

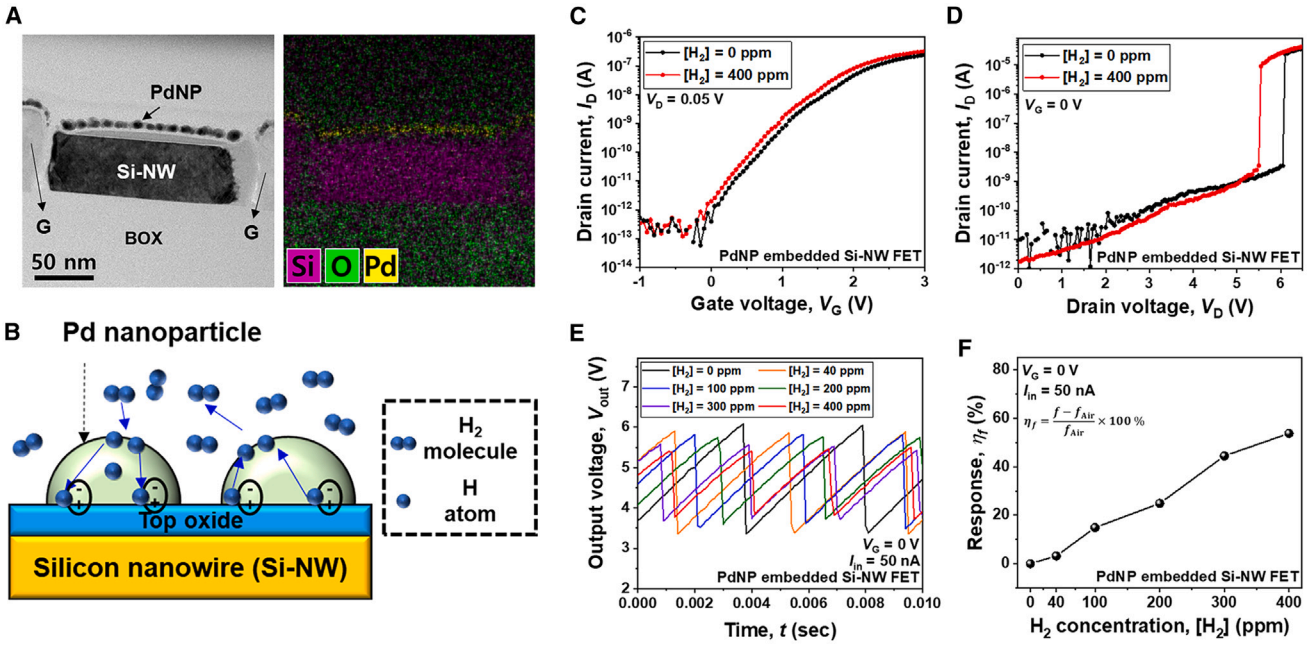

Figure 3. Si-NW FET embedded with palladium nanoparticles (PdNPs) for detecting hydrogen (H_2) gas

(A) Cross-sectional TEM image (left) and EDS mapping image (right) of the PdNP-embedded Si-NW.

(B) Detection mechanism of H_2 by the PdNP-embedded Si-NW FET. H_2 molecules are dissociated into H atoms, which diffuse through the Pd particles and then create dipoles at the interface between the Pd and the top oxide on the Si-NW.

(C) I_D-V_G characteristics. Positive poles oriented toward Si-NW lower V_T and accordingly raise I_D in the presence of H_2 gas.

(D) I_D-V_D characteristics. The positive poles pull down V_{latch} due to the reduced V_T with H_2.

(E) Spiking characteristic (V_{out}-time). $V_{T,firing}$ (=V_{top}) decreases and V_{bottom} increases with a high concentration of H_2.

(F) The response (η_f) increases as the H_2 concentration increases.

Characteristics of PdNP-embedded Si-NW FET for sensory neuron behaviors

Thermal oxide (SiO_2) was grown to 3 nm on the top of the exposed Si-NW before the formation of metal nanoparticles. This insulative SiO_2 prevents the metal nanoparticles from shorting electrically to the Si-NW channel. For the sensory neuron to detect H_2, catalytic Pd was physically deposited using an electron-beam evaporator. When the Pd thickness is 1 nm on the insulative SiO_2, the Pd atoms agglomerate, resulting in the formation of Pd nanoparticles (PdNPs) rather than a continuous film due to the low surface energy of SiO_2.[31,32] Figure 3A shows a cross-sectional image taken by a transmission electron microscope (TEM) along with the corresponding mapping image taken via energy-dispersive spectroscopy (EDS). The PdNPs were well formed on the top insulative oxide of the Si-NW FET.

Figure 3B illustrates the mechanism showing how the decorated PdNPs on the Si-NW FET sense H_2. When H_2 is absorbed at the surface of a PdNP, it dissociates into H. Then, the H diffuses into PdNP. The absorbed H forms electric dipoles at the interface between the Pd and SiO_2 layers, with the positive pole facing the underlying insulative SiO_2 on the Si-NW FET. As shown in Figure 3C, this positively aligned H dipole toward SiO_2 causes a negative shift of threshold voltage (V_T).[31,33] Here, V_T is used to discern whether an n-channel MOSFET with a p-type body is on or off. This reduced V_T causes more electrons to be injected into the p-type body, triggers the impact ionization to occur earlier, and eventually reduces V_{latch}, as shown in Figure 3D.[34] As a result, I_{latch} decreases in the presence of hydrogen gas.

With regard to sensitivity, Figure 3E shows the neuronal spiking operation of the sensory neuron with PdNPs for various concentrations of H_2. As explained above, more H_2 lowers V_{latch} and I_{latch}, which in turn lowers $V_{T,firing}$ due to reduced V_{latch} and raises V_{bottom} due to the reduced firing current. The tendency of f to become higher with a reduced $V_{T,firing}$ and an increased V_{bottom} was experimentally verified, as shown in Figure 3E, and can be understood through Equation 1. Herein, the sensing metric is defined as a response, $\eta_f = [(f - f_{air})/f_{air}] \cdot 100\%$, where f is the spiking frequency with H_2 and f_{air} is that without H_2, i.e., the spiking f with air. As shown in Figure 3F, η_f increases linearly with an increase in the H_2 concentration. This linearity, which is highly preferable to ensure a good sensor, is attractive for extrapolation as well as interpolation to predict H_2 concentrations even when there are no matching data between η_f and the H_2 concentration. A larger η_f is advantageous for higher sensitivity as a good biomimetic olfactory neuron.

In the proposed sensory neuron with PdNPs, η_f can be controlled by modulating V_G.[34] Because the abovementioned $V_{bi,S}$ is reduced to the increased V_G, more electrons are injected from S to the p-type body due to this enlarged V_G, with f then tending to increase even with a fixed H_2 concentration (e.g., Figure S4 shows that η_f becomes larger with an increase in V_G).

Please cite this article in press as: Lee et al., An artificial olfactory sensory neuron for selective gas detection with in-sensor computing, Device (2023), https://doi.org/10.1016/j.device.2023.100063

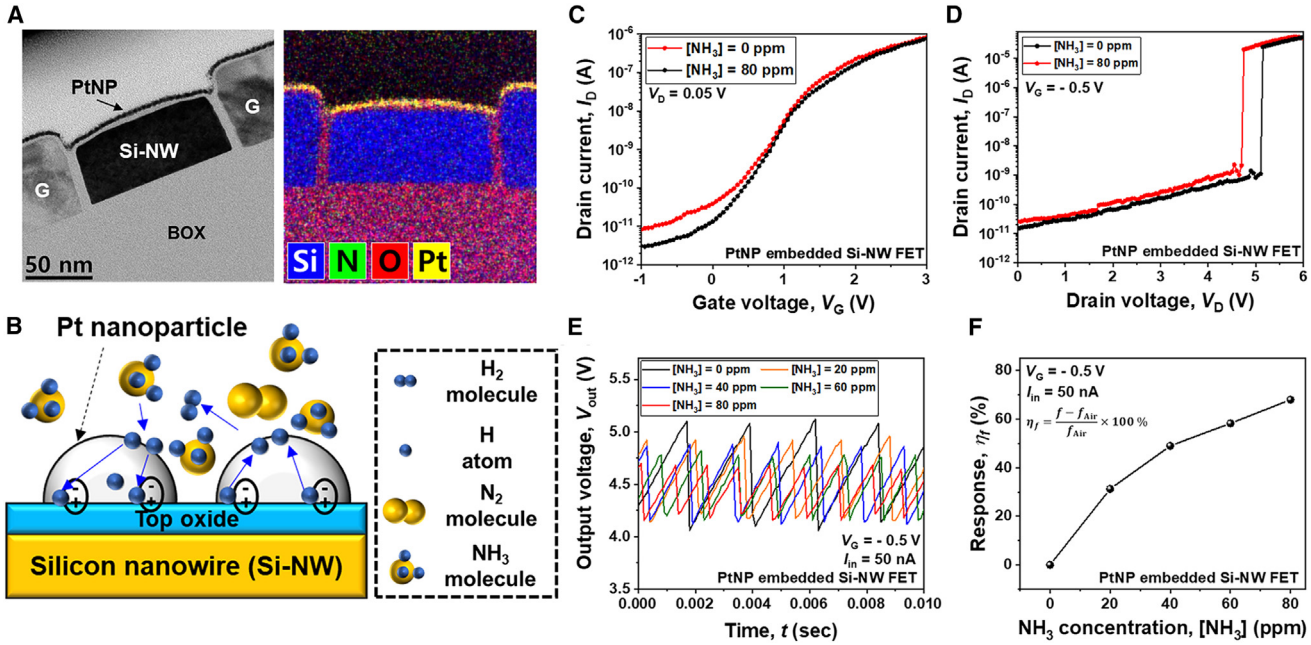

Figure 4. Si-NW FET embedded with PtNPs for sensing ammonia (NH_3) gas

(A) Cross-sectional TEM image (left) and EDS mapping image (right) of the PtNP-embedded Si-NW.

(B) Detection mechanism of NH_3 by the PtNP-embedded Si-NW FET. NH_3 molecules are dissociated into N_2 and H_2, and H_2 is then subsequently dissociated to H, which diffuses into the PtNP.

(C) I_D-V_G characteristics. Positive poles oriented toward Si-NW lower V_T and accordingly raise I_D in the presence of NH_3 gas.

(D) I_D-V_D characteristics. The positive poles pull down V_{latch} due to the reduced V_T with NH_3.

(E) Spiking characteristic (V_{out}-time). $V_{T,firing}$ (=V_{top}) decreases and V_{bottom} increases with a high concentration of NH_3.

(F) The response (η_f) increases as the NH_3 concentration increases.

Thereby, the sensory neuron with PdNPs senses H_2 gas from tens of ppm to 10,000 ppm by modulating the value of V_G for tunable sensitivity. Additionally, individual V_G control for each sensory neuron is useful to reduce the device-to-device fluctuation of η_f (see Figure S5). Conversely, the absence of a G is preferred to simplify metal interconnections in SNN if possible. When the body doping concentration is high enough in a Si-NW FET, keeping the channel in an off state becomes easier even without the presence of V_G, similar to an ungated or chemically gated FET.[25,35]

In terms of selectivity, Pd is known to exhibit high selectivity in detecting H_2 gas amid many other gases (see Figure S6 for η_f values for various types of gases).[36,37] The sensory neuron fabricated with PdNPs showed a high η_f value for only H_2 gas. Such selectivity is crucial when constructing a multiplexing sensor array expected to identify unknown gas mixtures.

Characteristics of PtNP-embedded Si-NW FET for sensory neuron behaviors

To demonstrate the ability of the sensor to distinguish different gases, NH_3, which has a decomposability similar to H_2, was selected as the other gas for the experiment. NH_3 was detected by a sensory neuron deposited with PtNPs instead of PdNPs. Akin to the fabrication procedure of the H_2 sensory neuron with PdNPs, Pt with a thickness of 1 nm was deposited onto the thermal oxide covering the exposed Si-NW using an electron-beam evaporator. Owing to the low surface energy of SiO_2, Pt tends to show island patterns instead of a continuous film. Figure 4A shows a cross-sectional TEM image and a corresponding EDS mapping image. NH_3 molecules decompose into N_2 and H_2 when catalyzed by PtNPs. The decomposed H_2 readily dissociates into H atoms on the PtNP surface and diffuses toward the oxide on the Si-NW.[38,39] Similar to the H dipole in the H_2 gas-sensing neuron with PdNPs, the H dipole stemming from NH_3 causes a negative shift of V_T and V_{latch}, as shown in Figures 4C and 4D, respectively. Being consistent with the H_2 sensory neuron with PdNPs, the tendency of f to increase with a reduction of $V_{T,firing}$ and an increase in V_{bottom} (see Equation 1) was observed in Figure 4E, due to the lowered V_{latch} and I_{latch}. As a result, Figure 4F shows that η_f increases with an increase in the NH_3 concentration. Similar to a PdNP-embedded Si-NW FET for sensing H_2, individually modulating V_G for each PtNP-embedded Si-NW FET for sensing NH_3 is helpful in suppressing the device-to-device fluctuation of η_f (see Figure S7).

The sensory neuron with PtNPs also responds directly to H_2 gas because of the dissociation of H_2 molecules into H atoms on its surface (see Figure S8). Therefore, sensors using Pt as a catalytic metal cannot easily classify H_2 gas and NH_3 gas due to their sensitivity to both gases. However, if the PtNP sensory neuron works with the PdNP sensory neuron to selectively detect H_2 via SNN, H_2 and NH_3 gases can be distinguished.

Please cite this article in press as: Lee et al., An artificial olfactory sensory neuron for selective gas detection with in-sensor computing, Device (2023), https://doi.org/10.1016/j.device.2023.100063

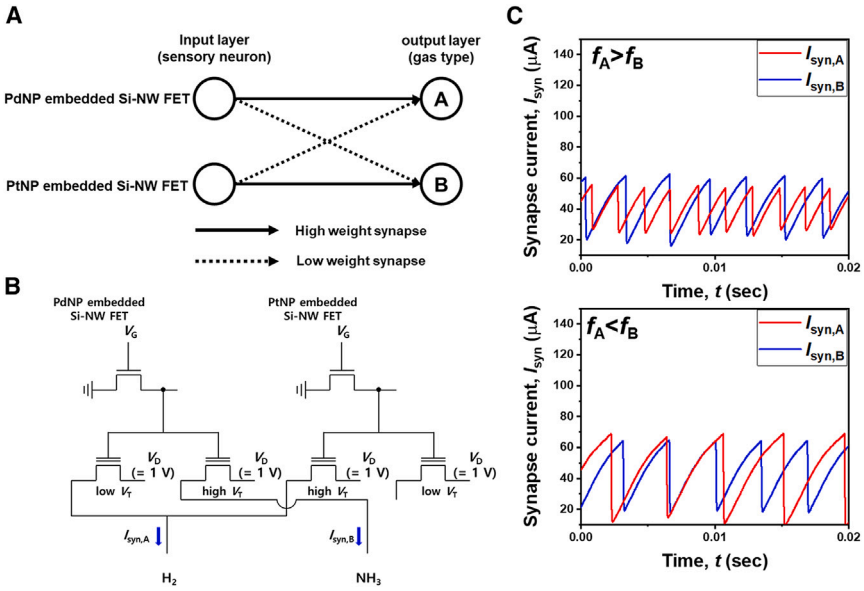

Figure 5. Gas classification with a catalytic metal-embedded Si-NW FET

(A) Configuration of a single-layer perceptron (SLP) for the classification of two gases. The input nodes corresponded to the catalytic metal-embedded Si-NW FET. The output layer has two nodes representing H_2 and NH_3.

(B) Circuit scheme for the gas-classification module. Spike signals are transferred to the gate electrode of the synapses, which are MOSFET-based flash memory devices. The V_T of the synapse represents the synaptic weight.

(C) Synapse current measured at output node A ($I_{syn,A}$) and output node B ($I_{syn,B}$). When H_2 gas was introduced, the spiking frequency of $I_{syn,A}$ was greater than $I_{syn,B}$. Otherwise, the frequency of $I_{syn,B}$ was greater than $I_{syn,A}$ when NH_3 gas was introduced.

Hardware implementation for gas classification

The process for producing the final data on the different gases is achieved using specific neuromorphic hardware for in-sensor computing using an SLP applied to an artificial neural network. The SLP consists of two sensory neurons as an input node and four synapses as an output node, as shown in Figure 5A. The input layer is composed of two sensory neurons, one with PdNPs and the other with PtNPs. As shown in Figure 5B, the former sensory neuron is connected to two synapses with low V_T and high V_T values. Like an artificial neuron, a synaptic device is also based on a MOSFET, where a charge-trap layer is intercalated into the G dielectrics. This synapse has a non-volatile memory function and is trainable through strengthening or weakening of the synaptic weight. Herein, the synaptic weight represents the connection between the input layer and the output layer and can be modulated by V_T in the case of a charge-trap-based flash memory device with a MOSFET structure.[40]

In this type of synapse, an increase in V_T for the depression operation is achieved by programming electrons to be trapped in the charge-trap layer, while a decrease in V_T for the potentiation operation is realized by erasing electrons that are de-trapped from the charge-trap layer (additional information regarding a synapse with a charge-trap-based flash memory is provided in Figure S9). This type of synapse, sometimes known by its abbreviation as SONOS, was fabricated on an SOI wafer like the sensory neuron and utilizes G dielectrics with three layers: SiO_2 as a blocking oxide (O), Si_3N_4 as a charge-trap layer (N), and SiO_2 as a tunneling oxide (O), which are in turn sandwiched between a poly-crystalline Si (S) G electrode and a single-crystalline Si (S) channel in an S-O-N-O-S stack formation. It should be noted that a sensory neuron and a synapse can be laterally co-integrated on the same plane or monolithically and vertically integrated on a different plane with the "synapse over neuron" structure.[27]

The output layer of SLP, consisting of four synapses, has two nodes: related to H_2 detection and relevant to NH_3 sensing. The sensory neuron with PdNPs has a strong connection to the synapse with a low V_T at the output node but a weak connection to the synapse with a high V_T at the output node. Conversely, the sensory neuron with PtNPs has a weak connection to the synapse with a high V_T at the output node but a strong connection to the synapse with a low V_T at the output node. It is well known that a lower V_T drives a higher I_D. Therefore, a synapse with a lower V_T has a stronger connecting weight. $I_{syn,A}$ with f_A is produced from the output node, while $I_{syn,B}$ with f_B comes from the output node. It is important to note that V_G of the sensory neuron with the PdNPs was 0 V and that with the PtNPs was −1 V, as the sensitivity can be controlled by modulating V_G and because the sensory neuron with the PdNPs is more sensitive to the H_2 gas in the proposed neuromorphic hardware. When H_2 gas is introduced, f_A is higher than f_B, as shown in Figure 5C. On the other hand, when NH_3 gas is introduced, f_B is higher than f_A, as shown in Figure 5D.

Although only two gases were classified using a very simple neural network structure in this work, it is possible to distinguish a more diverse gas mixture by adding a hidden layer in the form of an MLP or by increasing the temperature of a catalytic metal-embedded Si-NW FET through joule heating.[41–43] However, this expanded system will result in an exponential increase in the number of synapses, imposing a serious overload with increased power consumption on conventional von Neumann computing with a DNN. In contrast to this, power consumption is not a problem due to the inherent nature of low power consumption in the case of hardware-based SNN.

DISCUSSION

In this work, a two-in-one sensory neuron hybridizing a gas sensor and an artificial neuron was demonstrated using an SNN for in-sensor computing. Catalytic metal NPs deposited on the sensory neuron acted as a sensing component. When the sensory neuron decorated with metal NPs was exposed to a gas, the V_T shifted directly without the use of a transducer. This V_T shift in turn modulated an output spiking signal, which was then

directly delivered to the post-synapse without the aid of a current-to-voltage or voltage-to-current converter. Like a biological neuron, the fabricated sensory neuron showed LIF behavior, which is necessary for an SNN. The two-in-one sensory neuron can simultaneously perform sensing and spike encoding, which reduces its power requirements and hardware costs over other architectures that require external components such as an ADC, a processor, and memory units. Furthermore, certain manufacturing processes such as packaging and wire bonding are eliminated, meaning that the accompanying side effects can be avoided. In terms of electrical manipulation, the sensitivity of the artificial sensory neuron is tunable by adjusting the V_G. With regard to chemical specificity, the selectivity of the artificial sensory neuron is adjustable by changing the synaptic weight.

For multiplexing gas sensing, two types of gases (H_2 and NH_3) were distinguished using an SNN configuration in the form of SLP. The SNN consisted of two sensory neurons and four synapses. One sensory neuron was decorated with PdNPs for H_2 sensing, and the other sensory neuron was decorated with PtNPs for NH_3 and H_2 sensing. The sensory neurons and synapses were similar to each other in their use of MOSFET, but they were different because the neurons were decorated with metal particles on the top channel of the MOSFET, whereas the synapses harnessed a charge-trap layer in the G dielectrics. The combined device, with the incorporation of in-sensor computing, can quantitatively and selectively measure the concentrations of H_2 and NH_3 in the environment. The classification ability can be further improved by replacing the SLP with the MLP and creating a large array composed of a greater number of different sensory neurons with various sensing materials that react differently to specific gases. Due to the aforementioned low power consumption and small footprint area, a sensory neuron to realize in-sensor computing with the two-in-one structure is attractive for mobile and IoT devices. Thus, it can be used for detecting spoiled food, diagnosing diseases through breath tests, such as for lactose intolerance with H_2 and for kidney failure with NH_3, and improving safety in various environments by detecting explosive H_2 and harmful NH_3 in factories.

EXPERIMENTAL PROCEDURES

Resource availability

Lead contact

Further information and requests for resources should be directed to and will be fulfilled by the lead contact, Yang-kyu Choi (ykchoi@ee.kaist.ac.kr).

Materials availability

This study did not generate new unique reagents.

Data and code availability

Any additional information required to reanalyze the data reported in this paper is available from the lead contact upon request.

SUPPLEMENTAL INFORMATION

Supplemental information can be found online at https://doi.org/10.1016/j.device.2023.100063.

ACKNOWLEDGMENTS

This work was supported by the National R&D Program through the National Research Foundation of Korea (NRF) funded by the Ministry of Science (2018R1A2A3075302, 2021R1A2C300874213, 2021M3H4A3A0209921113, 2022M3F3A2A01072851, and RS-2023-00260637) and in part by the IC Design Education Center (EDA Tool and MPW).

AUTHOR CONTRIBUTIONS

S.-W.L. performed all experiments, analyzed the data, and wrote the paper. M.K. set up the gas chamber for gas detection and conducted gas experiments. J.-K.H. conceptualized the neuron-synapse configuration and interpreted the neuron-related data. S.-Y.Y. interpreted the neuron-related data. I.P. designed the gas detection apparatus and interpreted the sensor-related data. Y.-K.C. conceived the overall ideas and interpreted all the datasets.

DECLARATION OF INTERESTS

The authors declare no competing interests.

Received: June 7, 2023
Revised: July 3, 2023
Accepted: August 14, 2023
Published: September 5, 2023

REFERENCES

1. Gutmacher, D., Hoefer, U., and Wöllenstein, J. (2012). Gas sensor technologies for fire detection. Sensor. Actuator. B Chem. *175*, 40–45. https://doi.org/10.1016/j.snb.2011.11.053.
2. Yamazoe, N. (2005). Toward innovations of gas sensor technology. Sensor. Actuator. B Chem. *108*, 2–14. https://doi.org/10.1016/j.snb.2004.12.075.
3. Zhou, X., Xue, Z., Chen, X., Huang, C., Bai, W., Lu, Z., and Wang, T. (2020). Nanomaterial-based gas sensors used for breath diagnosis. J. Mater. Chem. B *8*, 3231–3248. https://doi.org/10.1039/C9TB02518A.
4. Berna, A. (2010). Metal Oxide Sensors for Electronic Noses and Their Application to Food Analysis. Sensors *10*, 3882–3910. https://doi.org/10.3390/s100403882.
5. Erbay, C., and Ergin, S. (2018). Random Number Generator Based on Hydrogen Gas Sensor for Security Applications. IEEE 61st International Midwest Symposium on Circuits and Systems (MWSCAS). https://doi.org/10.1109/MWSCAS.2018.8624016.
6. Gomes, J.B.A., Rodrigues, J.J.P.C., Rabêlo, R.A.L., Kumar, N., and Kozlov, S. (2019). IoT-Enabled Gas Sensors: Technologies, Applications, and Opportunities. J. Sens. Actuator Netw. *8*, 57. https://doi.org/10.3390/jsan8040057.
7. Suh, J.-H., Cho, I., Kang, K., Kweon, S.-J., Lee, M., Yoo, H.-J., and Park, I. (2018). Fully integrated and portable semiconductor-type multi-gas sensing module for IoT applications. Sensor. Actuator. B Chem. *265*, 660–667. https://doi.org/10.1016/j.snb.2018.03.099.
8. Hübert, T., Boon-Brett, L., Black, G., and Banach, U. (2011). Hydrogen sensors – A review. Sensor. Actuator. B Chem. *157*, 329–352. https://doi.org/10.1016/j.snb.2011.04.070.
9. Kwak, D., Lei, Y., and Maric, R. (2019). Ammonia gas sensors: A comprehensive review. Talanta *204*, 713–730. https://doi.org/10.1016/j.talanta.2019.06.034.
10. Zhang, J., Liu, X., Neri, G., and Pinna, N. (2016). Nanostructured Materials for Room-Temperature Gas Sensors. Adv. Mater. *28*, 795–831. https://doi.org/10.1002/adma.201503825.
11. Sysoev, V.V., Strelcov, E., Sommer, M., Bruns, M., Kiselev, I., Habicht, W., Kar, S., Gregoratti, L., Kiskinova, M., and Kolmakov, A. (2010). Single-Nanobelt Electronic Nose: Engineering and Tests of the Simplest Analytical Element. ACS Nano *4*, 4487–4494. https://doi.org/10.1021/nn100435h.
12. Sysoev, V.V., Goschnick, J., Schneider, T., Strelcov, E., and Kolmakov, A. (2007). A Gradient Microarray Electronic Nose Based on Percolating SnO2

Nanowire Sensing Elements. Nano Lett. *7*, 3182–3188. https://doi.org/10.1021/nl071815+.

13. MacNaughton, S., Sonkusale, S., Surwade, S., Ammu, S., and Manohar, S. (2011). Electronic nose based on graphene, nanotube and nanowire chemiresistor arrays on silicon. IEEE SENSORS Proceedings. https://doi.org/10.1109/ICSENS.2011.6127182.
14. Röck, F., Barsan, N., and Weimar, U. (2008). Electronic Nose: Current Status and Future Trends. Chem. Rev. *108*, 705–725. https://doi.org/10.1021/cr068121q.
15. Castro, M., Kumar, B., Feller, J.F., Haddi, Z., Amari, A., and Bouchikhi, B. (2011). Novel e-nose for the discrimination of volatile organic biomarkers with an array of carbon nanotubes (CNT) conductive polymer nanocomposites (CPC) sensors. Sensor. Actuator. B Chem. *159*, 213–219. https://doi.org/10.1016/j.snb.2011.06.073.
16. Zhang, L., and Tian, F. (2014). Performance Study of Multilayer Perceptrons in a Low-Cost Electronic Nose. IEEE Trans. Instrum. Meas. *63*, 1670–1679. https://doi.org/10.1109/TIM.2014.2298691.
17. Zhou, F., and Chai, Y. (2020). Near-sensor and in-sensor computing. Nat. Electron. *3*, 664–671. https://doi.org/10.1038/s41928-020-00501-9.
18. Merolla, P.A., Arthur, J.V., Alvarez-Icaza, R., Cassidy, A.S., Sawada, J., Akopyan, F., Jackson, B.L., Imam, N., Guo, C., Nakamura, Y., et al. (2014). A million spiking-neuron integrated circuit with a scalable communication network and interface. Science *345*, 668–673. https://doi.org/10.1126/science.1254642.
19. Davies, M., Srinivasa, N., Lin, T.-H., Chinya, G., Cao, Y., Choday, S.H., Dimou, G., Joshi, P., Imam, N., Jain, S., et al. (2018). Loihi: A Neuromorphic Manycore Processor with On-Chip Learning. IEEE Micro *38*, 82–99. https://doi.org/10.1109/MM.2018.112130359.
20. Kwon, D., Jung, G., Shin, W., Jeong, Y., Hong, S., Oh, S., Kim, J., Bae, J.-H., Park, B.-G., and Lee, J.-H. (2021). Efficient fusion of spiking neural networks and FET-type gas sensors for a fast and reliable artificial olfactory system. Sensor. Actuator. B Chem. *345*, 130419. https://doi.org/10.1016/j.snb.2021.130419.
21. Han, J.K., Kang, M., Jeong, J., Cho, I., Yu, J.M., Yoon, K.J., Park, I., and Choi, Y.K. (2022). Artificial Olfactory Neuron for an In-Sensor Neuromorphic Nose. Adv. Sci. *9*, 2106017. https://doi.org/10.1002/advs.202106017.
22. Wang, T.K.M., Unai, S., Xu, B., and Guo, X. (2021). An artificial olfactory inference system based on memristive devices. InfoMat *11*, 804–817. https://doi.org/10.1002/inf2.12196.
23. Rana, S.V., and Malik, A. (2014). Hydrogen Breath Tests in Gastrointestinal Diseases. Indian J. Clin. Biochem. *29*, 398–405. https://doi.org/10.1007/s12291-014-0426-4.
24. Lefferts, M.J., and Castell, M.R. (2022). Ammonia breath analysis. Sens. Diagn. *1*, 955–967. https://doi.org/10.1039/D2SD00089J.
25. Han, J.-W., and Meyyappan, M. (2018). Leaky Integrate-and-Fire Biristor Neuron. IEEE Electron. Device Lett. *39*, 1457–1460. https://doi.org/10.1109/LED.2018.2856092.
26. Han, J.-K., Seo, M., Kim, W.-K., Kim, M.-S., Kim, S.-Y., Kim, M.-S., Yun, G.-J., Lee, G.-B., Yu, J.-M., and Choi, Y.-K. (2020). Mimicry of Excitatory and Inhibitory Artificial Neuron With Leaky Integrate-and-Fire Function by a Single MOSFET. IEEE Electron. Device Lett. *41*, 208–211. https://doi.org/10.1109/LED.2019.2958623.
27. Han, J.-K., Oh, J., Yun, G.-J., Yoo, D., Kim, M.-S., Yu, J.-M., Choi, S.-Y., and Choi, Y.-K. (2021). Cointegration of single-transistor neurons and synapses by nanoscale CMOS fabrication for highly scalable neuromorphic hardware. Sci. Adv. *7*, eabg8836. https://doi.org/10.1126/sciadv.abg8836.
28. Han, J.-K., Seo, M., Yu, J.-M., Suh, Y.-J., and Choi, Y.-K. (2020). A Single Transistor Neuron With Independently Accessed Double-Gate for Excitatory-Inhibitory Function and Tunable Firing Threshold Voltage. IEEE Electron. Device Lett. *41*, 1157–1160. https://doi.org/10.1109/LED.2020.3001953.
29. Han, J.-K., Geum, D.-M., Lee, M.-W., Yu, J.-M., Kim, S.K., Kim, S., and Choi, Y.-K. (2020). Bioinspired Photoresponsive Single Transistor Neuron for a Neuromorphic Visual System. Nano Lett. *20*, 8781–8788. https://doi.org/10.1021/acs.nanolett.0c03652.
30. Yun, S.-Y., Han, J.-K., Lee, S.-W., Yu, J.-M., Jeon, S.-B., and Choi, Y.-K. (2023). Self-aware artificial auditory neuron with a triboelectric sensor for spike-based neuromorphic hardware. Nano Energy *109*, 108322. https://doi.org/10.1016/j.nanoen.2023.108322.
31. Ahn, J.-H., Yun, J., Choi, Y.-K., and Park, I. (2014). Palladium nanoparticle decorated silicon nanowire field-effect transistor with side-gates for hydrogen gas detection. Appl. Phys. Lett. *104*, 013508. https://doi.org/10.1063/1.4861228.
32. Yun, J., Ahn, J.-H., Moon, D.-I., Choi, Y.-K., and Park, I. (2019). Joule-Heated and Suspended Silicon Nanowire Based Sensor for Low-Power and Stable Hydrogen Detection. ACS Appl. Mater. Interfaces *11*, 42349–42357. https://doi.org/10.1021/acsami.9b15111.
33. Lundström, K.I., Shivaraman, M.S., and Svensson, C.M. (1975). A hydrogen-sensitive Pd-gate MOS transistor. J. Appl. Phys. *46*, 3876–3881. https://doi.org/10.1063/1.322185.
34. Han, J.-K., Park, S.-C., Yu, J.-M., Ahn, J.-H., and Choi, Y.-K. (2022). A Bio-inspired Artificial Gustatory Neuron for a Neuromorphic Based Electronic Tongue. Nano Lett. *22*, 5244–5251. https://doi.org/10.1021/acs.nanolett.2c01107.
35. Han, J.-W., Rim, T., Baek, C.-K., and Meyyappan, M. (2015). Chemical Gated Field Effect Transistor by Hybrid Integration of One-Dimensional Silicon Nanowire and Two-Dimensional Tin Oxide Thin Film for Low Power Gas Sensor. ACS Appl. Mater. Interfaces *7*, 21263–21269. https://doi.org/10.1021/acsami.5b05479.
36. Darmadi, I., Nugroho, F.A.A., and Langhammer, C. (2020). High-Performance Nanostructured Palladium-Based Hydrogen Sensors—Current Limitations and Strategies for Their Mitigation. ACS Sens. *5*, 3306–3327. https://doi.org/10.1021/acssensors.0c02019.
37. Cho, M., Kim, T., Cho, I., Gao, M., Kang, K., Yang, D., and Park, I. (2022). Nanogap Formation Using a Chromium Oxide Film and Its Application as a Palladium Hydrogen Switch. Langmuir *38*, 1072–1078. https://doi.org/10.1021/acs.langmuir.1c02643.
38. Ross, J.F., Robins, I., and Webb, B.C. (1987). The ammonia sensitivity of platinum-gate MOSFET devices: dependence on gate electrode morphology. Sensor. Actuator. *11*, 73–90. https://doi.org/10.1016/0250-6874(87)85006-0.
39. Safari, M., Gholizadeh, M., and Salehi, A. (2009). Modeling and simulation of a MOSFET gas sensor with platinum gate for hydrogen gas detection. Sensor. Actuator. B Chem. *141*, 1–6. https://doi.org/10.1016/j.snb.2009.06.032.
40. Choi, H.-S., Kim, H., Lee, J.-H., Park, B.-G., and Kim, Y. (2020). AND Flash Array Based on Charge Trap Flash for Implementation of Convolutional Neural Networks. IEEE Electron. Device Lett. *41*, 1653–1656. https://doi.org/10.1109/LED.2020.3025587.
41. Ackelid, U., Armgarth, M., Spetz, A., and Lundstrom, I. (1986). Ethanol sensitivity of palladium-gate metal-oxide-semiconductor structures. IEEE Electron. Device Lett. *7*, 353–355. https://doi.org/10.1109/EDL.1986.26398.
42. Winquist, F., and Lundström, I. (1987). Thin metal film—oxide—semiconductor structures with temperature-dependent sensitivity for unsaturated hydrocarbons. Sensor. Actuator. *12*, 255–261. https://doi.org/10.1016/0250-6874(87)80039-2.
43. Park, J.-Y., Moon, D.-I., Seol, M.-L., Kim, C.-K., Jeon, C.-H., Bae, H., Bang, T., and Choi, Y.-K. (2016). Self-Curable Gate-All-Around MOSFETs Using Electrical Annealing to Repair Degradation Induced From Hot-Carrier Injection. IEEE Trans. Electron. Dev. *63*, 910–915. https://doi.org/10.1109/TED.2015.2513744.